RSC Advances

PAPER

View Article Online
View Journal | View Issue

Cite this: *RSC Adv.*, 2026, **16**, 12348

Tailoring hydrogenation, thermodynamic properties and oxidation resistance of TiFe alloy by only regulating the stoichiometric ratio of Ti and Fe elements

Siqi Xia,[acd] Guojie Wu,[acd] Dongfang Huang,*[abc] Guixiang Ma,[b] Haonan Cai,[cd] Jinyuan Jiang,[ce] Quanbao Zhou,[e] Xuebo Yan[a] and Peng Lv *[acd]

This study systematically investigates the effect of regulating the stoichiometric ratio of Ti and Fe elements on the microstructure, hydrogenation properties, thermodynamics and oxidation resistance of Ti_xFe_{2-x} (x = 1, 1.1, 1.2, 1.3) alloys. Microstructural analysis reveals that all as-cast alloys except $x = 1$ alloy consist of a TiFe main phase and Ti_2Fe secondary phase. Increasing Ti content leads to the expansion of the lattice parameters, unit cell volume and crystallite size of the TiFe phase, alongside an increase in the area percentage of a dark phase observed in the microstructure. Regarding hydrogenation, higher Ti content enhances first hydrogenation kinetics and increases the maximum hydrogen storage capacity from 1.91 wt% (x = 1.1) to 2.27 wt% (x = 1.3), which is attributed to the dark phase facilitating hydrogen dissociation and diffusion. However, the reversible hydrogen storage capacity decreases from 1.37 wt% (x = 1.1) to 1.10 wt% (x = 1.3), likely due to the formation of stable TiH_x hydrides. Thermodynamically, the activation energy of hydrogen absorption decreases with higher Ti content (from 18.62 kJ mol^{-1} of x = 1.1 to 11.97 kJ mol^{-1} of x = 1.3), indicating enhanced hydrogen diffusion. Conversely, the activation energy of hydride decomposition and the hydride stability increases with Ti content. Furthermore, the oxidation resistance of the alloys deteriorates as Ti content increases, ascribed to the higher oxidation sensitivity of Ti compared to Fe.

Received 4th December 2025
Accepted 23rd February 2026

DOI: 10.1039/d5ra09388k

rsc.li/rsc-advances

1 Introduction

With the growing severity of global environmental issues and the continuous depletion of fossil fuels, the search for alternative energy sources has become a key priority for countries worldwide to address the energy crisis.[1,2] As a crucial component of clean energy, hydrogen energy has attracted widespread attention. However, its large-scale utilization strongly depends on breakthroughs in hydrogen storage and transportation technologies.[3,4] Hydrogen storage alloys can absorb hydrogen at relatively low hydrogen pressure and temperature, which fundamentally overcomes the limitations of conventional high pressure gaseous and cryogenic liquid hydrogen storage methods.[5] Among all hydrogen storage alloys, TiFe alloy has been extensively investigated owing to its better hydrogen storage properties including a maximum hydrogen storage capacity of approximately 1.86 wt% and a long cycle life. In addition, it also can absorb hydrogen at room temperature and relatively low hydrogen pressure.[6]

Although TiFe hydrogen storage alloy has a broad application prospect, it still faces several problems that need to be solved. The main problems are difficulty in activation and susceptibility to oxidation. Many methods including elemental doping,[7–14] mechanical deformation[15–17] and surface treatment[18,19] have been applied to overcome these problems. Among all methods, elemental doping is an effective way to improve the hydrogen storage properties of TiFe alloy. For instance, Mn element can be introduced into TiFe alloy. BARALE Jb *et al.*[7] reported that TiFe alloy doped with Mn exhibited a hydrogen storage capacity of 1.0 wt% at 55 °C and 25 bar hydrogen pressure. This alloy not only showed excellent hydrogen adsorption/desorption kinetics but also showed good oxidation resistance. Park *et al.*[20] synthesized $TiFe_{1-x}Mn_x$ alloys and found that the incubation time of $TiFe_{0.7}Mn_{0.3}$ alloy was significantly shortened from 300 to 20 min during the first hydrogenation process. Elements such as Zr/Hf/Cr/Mo, *etc.* were

[a]*Engineering Research Center of Nuclear Technology Application (East China University of Technology), Ministry of Education, Nanchang, 330013, China. E-mail: h-348931432@ecut.edu.cn; lvpeng@ecut.edu.cn*

[b]*School of Science, East China University of Technology, 330013, China*

[c]*School of Water Resources and Environmental Engineering, East China University of Technology, Nanchang 330013, Jiangxi, China*

[d]*Jiangxi Provincial Key Laboratory of Genesis and Remediation of Groundwater Pollution (East China University of Technology), Nanchang 330013, Jiangxi, China*

[e]*School of Chemistry and Materials Science, East China University of Technology, Nanchang 330013, Jiangxi, China*

also introduced into TiFe alloy. Gosselin *et al.*[10] found that TiFe + 4 wt% Zr alloy could absorb hydrogen directly without any treatment at room temperature and 45 bar hydrogen pressure. In addition, the presence of Zr rich intergranular phases $(Ti_{1-y}Zr_y)_2Fe$ was identified, which effectively addressed the issue of hard activation of TiFe alloy. Razafindramanana *et al.*[11] reported that the addition of 8 wt% Hf was the minimum limit for activating TiFe alloy without any treatment at room temperature and 20 bar hydrogen pressure. The three-phase structure (B2-TiFe, Fe-rich C14-Laves phase and Ti-rich BCC phase) induced by Hf may be the core of properties enhancement. Jung *et al.*[13] reported that TiFe alloy doped with Cr contained Ti(Cr, Fe)$_2$ phase that is helpful for improving the first hydrogen absorption kinetics. But the maximum hydrogen storage capacity decreased with increasing the fraction of Ti(Cr, Fe)$_2$ phase. Li *et al.*[14] synthesized a series of quaternary $Ti_{1.05}Fe_{0.85}Cr_{0.1-x}Mo_x$ alloys. All alloys can absorb hydrogen at room temperature without any treatment and $TiFe_{0.85}Cr_{0.05}Mo_{0.05}$ alloy showed the best hydrogen storage properties. Except for elemental doping, mechanical deformation and surface treatment were also employed to handle TiFe alloy. Manna *et al.*[15] used ball milling to improve the first hydrogenation kinetics of TiFe alloy. After ball milling, the alloy absorbed 1.5 wt% hydrogen without any treatment during the first hydrogenation. Vega *et al.*[17] reported that cold rolled treatment enhanced the first hydrogenation of TiFe alloy and the maximum hydrogen storage capacity reached 1.4 wt%. Davids *et al.*[18] carried out metal organic chemical vapour deposition technique to synthesized a Pd film on the surface of TiFe alloy and found that Pd coated TiFe alloy showed good oxidation resistance. Peng *et al.*[19] used chemical plating to prepare Ni coated $TiFe_{0.8}Mn_{0.15}Zr_{0.05}$ alloy. They found that the alloy with Ni plating for 10 min exhibited rapid first hydrogen absorption kinetics and the best oxidation resistance.

Although techniques such as element doping, mechanical modification and surface treatment can improve the hydrogen storage properties of TiFe alloy, they often suffer from drawbacks including high cost and complex processing. Several studies have attempted to enhance the hydrogen storage properties of TiFe alloy by regulating stoichiometric ratio of Ti and Fe elements. K. B. Park *et al.*[21] conducted preliminary studies on the hydrogen absorption kinetics of $Ti_{1.2}Fe$ alloy and suggested that Ti_2Fe phase might promote hydrogenation. Later, Ulate-Kolitsky *et al.*[22] synthesized $Ti_{1.2}Fe_{0.8}$ alloy by arc melting and found that the alloy can absorb hydrogen within 12 h without any heat treatment or mechanical processing due to the finer distribution of secondary phases (Ti_2Fe and BCC). However, these earlier works focused only on single-composition alloys and the research on hydrogen storage properties is not comprehensive. In order to gain a deeper understanding of the effects of regulating stoichiometric ratio of Ti and Fe elements on the microstructure, hydrogen storage properties, thermodynamic properties and oxidation resistance of TiFe alloy. The Ti_xFe_{2-x} ($x = 1, 1.1, 1.2, 1.3$) alloys are designed and prepared by arc melting.

2 Experimental details

High-purity metal raw materials of Ti and Fe (99.9%) were supplied by ZhongNuo Advanced Material (Beijing) Technology Co., Ltd. The total mass of the raw materials was 3 g and each element was weighed precisely according to the designed stoichiometric ratio. The mixture was placed in a water-cooled copper crucible and melted under a high-purity argon atmosphere using an arc-melting furnace (SP-MSM207) provided by Shenyang Kejing Instrument Co., Ltd. During arc melting, the ingots were remelted four times by flipping to ensure compositional homogeneity of Ti_xFe_{2-x} ($x = 1, 1.1, 1.2, 1.3$) alloys. After solidification, the ingots were mechanically crushed using a steel mortar and sieved to obtain alloy powder with particle size ranging from 50–80 mesh.

The phase structure of all alloys before and after hydrogenation was characterized by XRD (Bruker D8 Advance, Cu Kα). The morphology was observed by scanning electron microscopy (SEM, FEI Nova NanoSEM 450). Thermal analysis of both hydrogenated and dehydrogenated alloys was carried out by using a HITACHI STA 200 thermal analyzer under a flow of pure nitrogen at different heating rates. Additionally, TGA was performed on the same HITACHI STA 200 instrument in air to assess the oxidation behavior of the alloys. In order to evaluate the hydrogen storage properties, a home-made Sieverts-

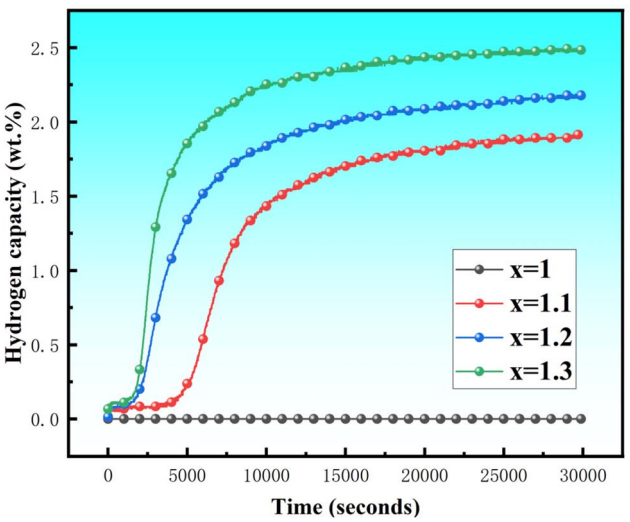

Fig. 1 First hydrogenation curves of Ti_xFe_{2-x} ($x = 1, 1.1, 1.2, 1.3$) alloys at 30 °C and under 20 bar.

Table 1 The incubation time and maximum hydrogen storage capacity of different alloys during the first hydrogenation

Sample	Incubation time (s)	Maximum hydrogen storage capacity (wt%)
$x = 1$	—	—
$x = 1.1$	4200	1.91
$x = 1.2$	1893	2.07
$x = 1.3$	1177	2.27

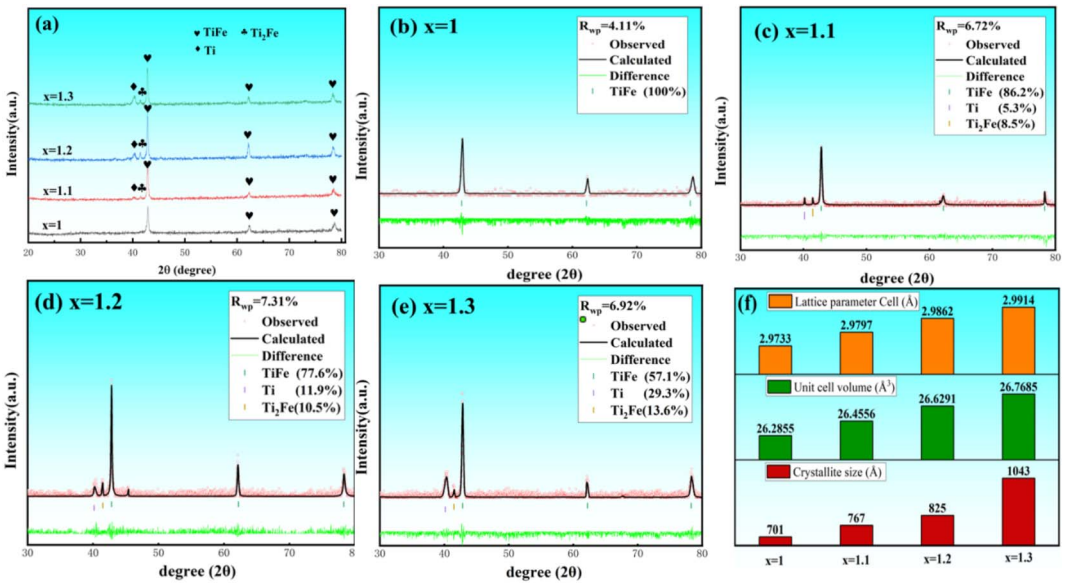

Fig. 2 XRD patterns of all as-cast Ti_xFe_{2-x} ($x = 1, 1.1, 1.2, 1.3$) alloys (a). Rietveld refinement curves of all as-cast Ti_xFe_{2-x} ($x = 1, 1.1, 1.2, 1.3$) alloys (b–e). Some structural parameters of TiFe phase obtained from Rietveld refinement (f).

type apparatus was used. The hydrogen absorption was performed at 30 °C under 20 bar. Prior to each hydrogenation process, the system was evacuated for 30 minutes by using a vacuum pump.

3 Results and discussion

3.1 First hydrogenation properties

Fig. 1 presents the first hydrogenation curves of Ti_xFe_{2-x} ($x = 1$, 1.1, 1.2, 1.3) alloys measured at 30 °C under 20 bar. It is clear

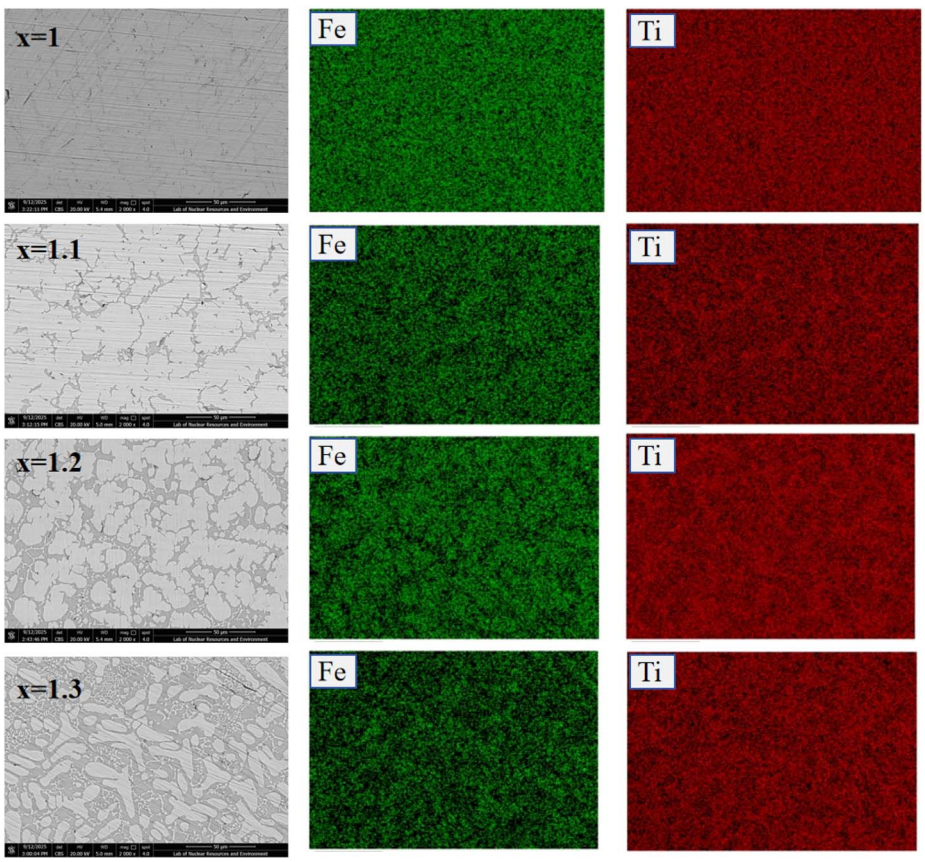

Fig. 3 BSE images and EDS mapping of Ti_xFe_{2-x} ($x = 1, 1.1, 1.2, 1.3$) alloys in 50 μm.

Table 2 The composition of Ti_xFe_{2-x} (x = 1, 1.1, 1.2, 1.3) alloys

Samples	Theoretical Ti content (atomic. %)	Theoretical Fe content (atomic. %)	Actual Ti content (atomic. %)	Actual Fe content (atomic. %)
$x = 1$	50.00	50.00	51.19	48.81
$x = 1.1$	55.00	45.00	55.90	44.10
$x = 1.2$	60.00	40.00	60.89	39.11
$x = 1.3$	65.00	35.00	65.40	34.60

that, except for the $x = 1$ alloy (pure TiFe alloy), all alloys can absorb hydrogen directly after different incubation time without any prior activation or external surface treatment. Table 1 shows the incubation time and maximum hydrogen storage capacity of different alloys during the first hydrogenation. It is clear that the incubation time reduces significantly from 4200 s of $x = 1.1$ alloy to 1177 s of $x = 1.3$ alloy and the maximum hydrogen storage capacity increases from 1.91 wt% of $x = 1.1$ alloy to 2.27 wt% of $x = 1.3$ alloy. In addition, the first hydrogenation kinetics also rises with increasing x from 1.1 to 1.3. This result suggests that the partial substitution of Fe by Ti can facilitate hydrogen diffusion during first hydrogenation process effectively.

3.2 XRD pattern

XRD patterns of all as-cast alloys are shown in Fig. 2(a). It is clear that all as-cast alloys exhibit TiFe as the primary phase and Ti_2Fe as the secondary phase, except for the $x = 1$ alloy, which contains only TiFe phase. With Ti content increases, the intensity of these diffraction peaks corresponding to Ti_2Fe phase becomes increasingly pronounced. The presence of Ti_2Fe phase maybe the reason why $x = 1.1$, 1.2 and 1.3 alloys can absorb hydrogen directly under 20 bar hydrogen pressure without any activation treatment. Park *et al.*[21] reported that higher Ti content promoted the formation of Ti_2Fe and Ti_4Fe phases, providing diffusion pathways for hydrogen and improving hydrogen absorption kinetics of the alloy.

Fig. 2(f) shows the lattice parameter, unit cell volume and crystallite size of all as-cast alloys obtained from Rietveld refinement of Fig. 2(b–e). With increasing Ti content, the lattice parameter of TiFe phase increases from 2.9733 Å ($x = 1$) to 2.9914 Å ($x = 1.3$) and the unit cell volume increases from 26.29 $Å^3$ to 26.77 $Å^3$. Meanwhile, the crystallite size increases from 701 Å to 1043 Å. This expansion of lattice parameter and unit cell volume may be attributed to the larger atomic radius of Ti (1.47 Å) compared with Fe (1.26 Å). The above results may be one of the reasons for the improved hydrogen absorption properties of the alloy.

3.3 Morphology

Fig. 3 shows the BSE images and EDS mapping of Ti_xFe_{2-x} (x = 1, 1.1, 1.2, 1.3) alloys in 50 μm. It can be seen clearly that all

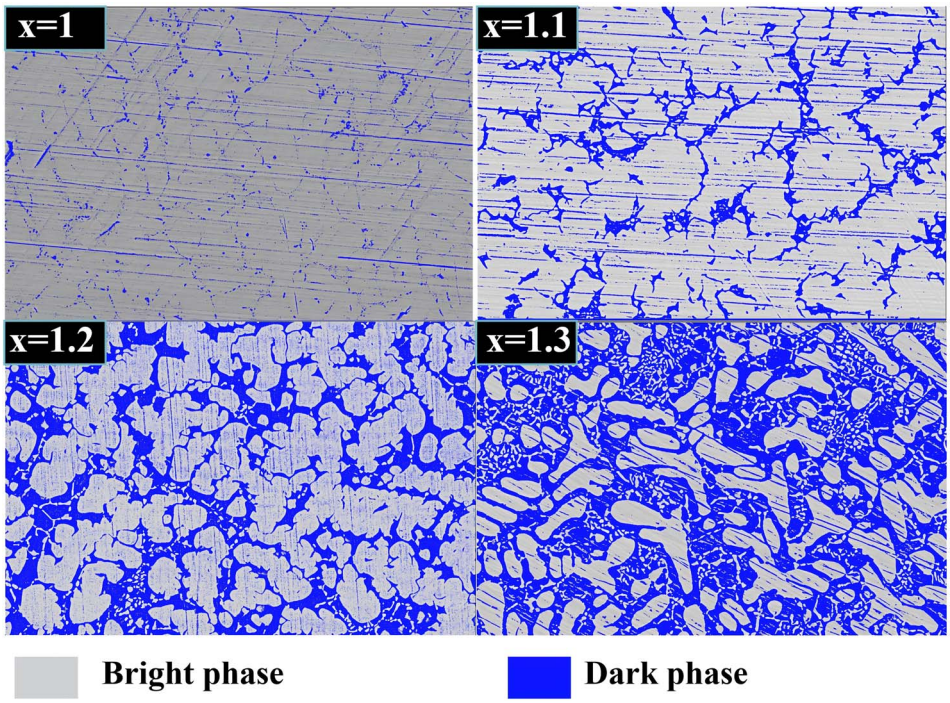

Fig. 4 The area percentage of two phases of Ti_xFe_{2-x} (x = 1, 1.1, 1.2, 1.3) alloys.

Table 3 The area percentage of the bright phase and dark phase

Sample	Bright phase (%)	Dark phase (%)
$x = 1$	93.31	6.69
$x = 1.1$	80.82	19.18
$x = 1.2$	64.83	35.17
$x = 1.3$	51.14	48.86

alloys consist of two regions with distinct contrast, appearing as bright and dark phases. In the bright phase, Ti and Fe elements are uniformly distributed. In the dark phase, there is a higher concentration of Ti element and a lower concentration of Fe element. In addition, there is a notable increase in the number of interfaces including grain boundaries between two phases. Such grain boundaries can provide effective diffusion channels for hydrogen and reduce the incubation time during the first hydrogenation.[16,23,24] Table 2 presents the composition of Ti_x-Fe_{2-x} ($x = 1, 1.1, 1.2, 1.3$) alloys. It is clear that the actual content of Ti and Fe is close to the theoretical content of Ti and Fe.

In order to compare the area percentage of different phases, the BSE images of all alloys are processed by using Image J software. The dark phase is marked with blue color in Fig. 4. The area percentage of the bright phase and dark phase obtained from Fig. 4 is shown in Table 3. It is clear that the area percentage of the dark phase rises with the increase of Ti content.

Fig. 5 presents the composition of the bright and dark phases as quantified by EDS pointing analysis, where points A and B represent the bright phase and dark phase, respectively. The corresponding composition of point A and B is summarized in Table 4. It is very clear that Ti content is always higher that Fe content in both phases. In the bright phase, the atomic ratio of Ti to Fe is close. But in the dark phase, the atomic ratio of Ti to Fe is close to 3 : 1 except pure TiFe alloy ($x = 1$). This result means that the bright phase may be mainly composed of TiFe phase and the dark phase may be a mixture of TiFe and Ti_2Fe phases.

Table 4 The composition of point A and B obtained from Fig. 5

Samples	Element	Bright phase (atomic. %)	Dark phase (atomic. %)
$x = 1$	Ti	50.39	50.36
	Fe	49.61	49.64
$x = 1.1$	Ti	52.07	76.86
	Fe	47.93	23.14
$x = 1.2$	Ti	51.97	77.02
	Fe	48.03	22.98
$x = 1.3$	Ti	52.56	77.49
	Fe	47.44	22.51

3.4 Hydrogenation cycles

The hydrogenation cycles of Ti_xFe_{2-x} ($x = 1.1, 1.2, 1.3$) alloys are shown in Fig. 6(a–c). The maximum and reversible hydrogen storage capacities are shown in Fig. 6(d). It is clear that the reversible hydrogen storage capacity of each alloy keeps stable but is lower than the maximum hydrogen storage capacity of the first hydrogenation. With increasing Ti content, the reversible hydrogen storage capacity decreases from 1.37 wt% ($x = 1.1$) to 1.10 wt% ($x = 1.3$). Especially the $x = 1.3$ alloy shows the greatest loss in reversible hydrogen storage capacity (about 1.17 wt%). This reversible hydrogen storage capacity loss is mainly caused by the excessive Ti reacting with hydrogen to form stable TiH_x hydrides. These TiH_x hydrides show thermodynamic stability and are not prone to decomposition at room temperature. Fig. 7 shows the variation of hydrogen storage capacity retention with different Ti_2Fe content. It is clear that the hydrogen storage capacity retention of the alloy significantly decreases with increasing the content of Ti_2Fe phase. In

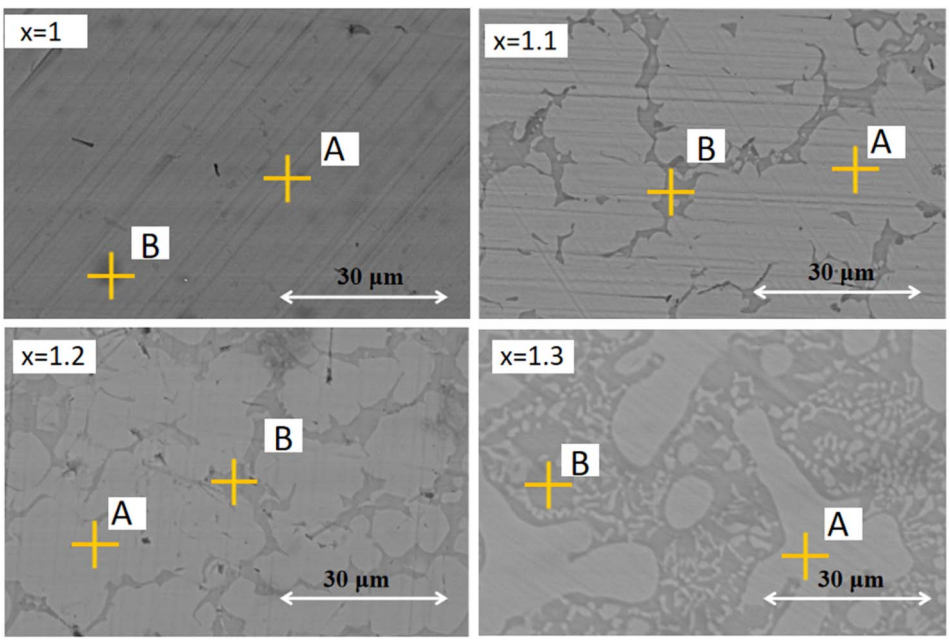

Fig. 5 The BSE images of Ti_xFe_{2-x} ($x = 1, 1.1, 1.2, 1.3$) alloys in 30 μm.

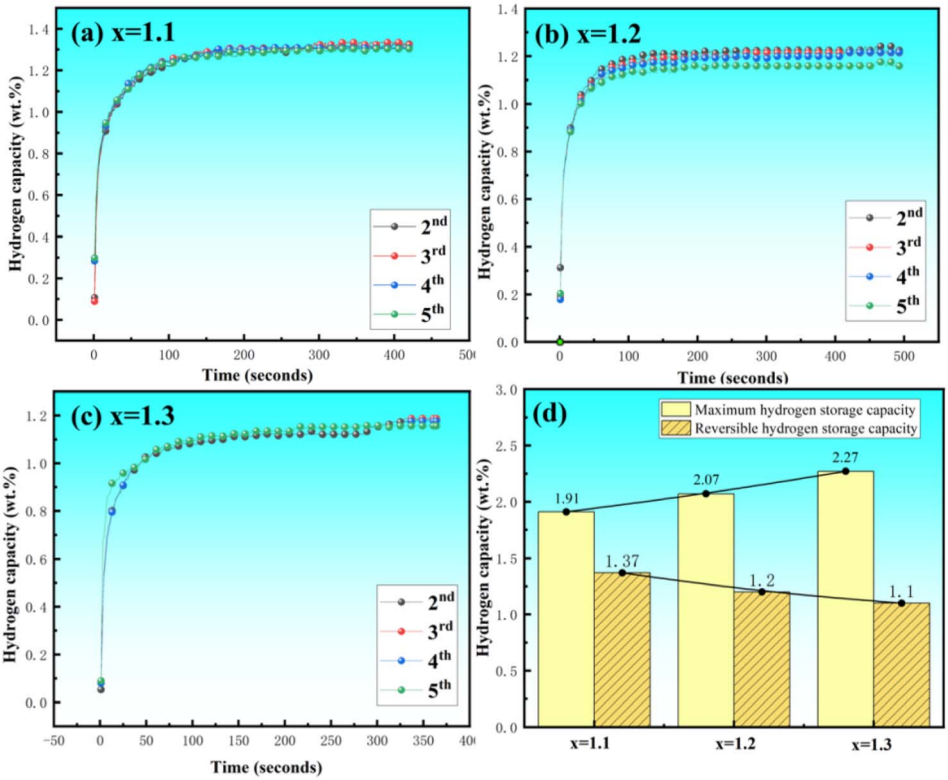

Fig. 6 Hydrogenation cycles (from 2nd to 5th) of Ti_xFe_{2-x} ($x = 1.1, 1.2, 1.3$) alloys at room temperature and under 20 bar hydrogen pressure (a–c). The maximum and reversible hydrogen storage capacities in the first hydrogen hydrogenation of all alloys (d).

addition, the content of Ti_2Fe phase increases from 8.5% to 13.6% with x from 1.1 to 1.3 in Fig. 2. This result indicates that the formation of Ti_2Fe is associated with the reduction of the reversible hydrogen storage capacity of the alloy.

In order to investigate the composition of the irreversible hydrides that are difficult to decompose at room temperature, XRD was performed for all dehydrogenated alloys in Fig. 8. It is clear that the dehydrogenated alloy mainly consists of TiFe, Ti_2Fe, TiH_x and FCC phases. The presence of TiFe phase may be due to the decomposition of $TiFeH_x$ at room temperature. The formation of TiH_x is attributed to the reaction between excess Ti and hydrogen leading to the irreversible hydrides that are difficult to decompose at room temperature.

Based on the above results, the predicted mechanism of hydrogen absorption Ti_xFe_{2-x} ($x = 1.1, 1.2, 1.3$) alloys can be illustrated in Fig. 9. As shown in Fig. 3, all alloys consist of the bright and dark phases. During the process of hydrogen absorption, hydrogen molecules dissociate into atoms on the surface of the dark phase. Then these hydrogen atoms can

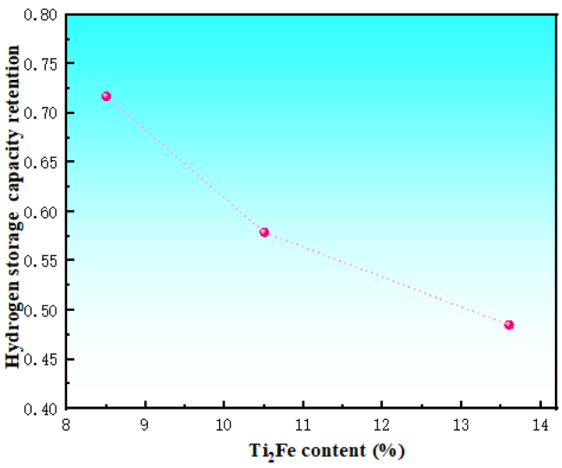

Fig. 7 The variation of hydrogen storage capacity retention with Ti_2Fe content.

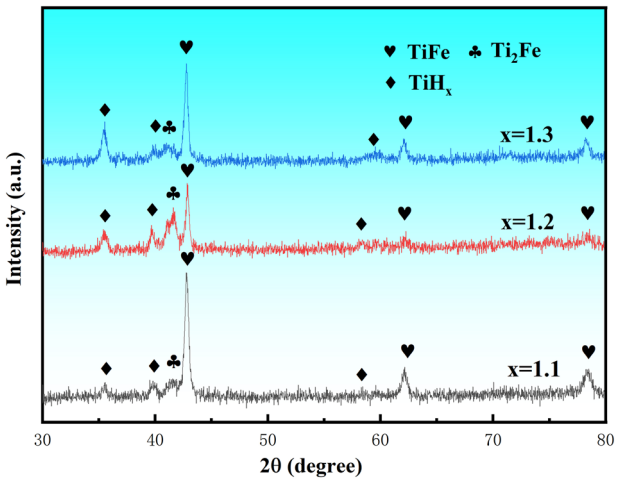

Fig. 8 XRD pattern of Ti_xFe_{2-x} ($x = 1.1, 1.2, 1.3$) alloys after dehydrogenation.

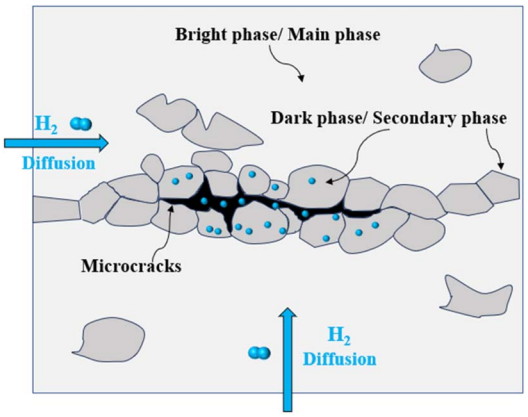

Fig. 9 Prediction mechanism of hydrogen absorption of Ti_xFe_{2-x} (x = 1.1, 1.2, 1.3) alloys.

rapidly diffuse through the dark phase and migrate into the interior of the alloy, resulting in the formation of numerous microcracks. These microcracks could provide pathways for hydrogen atoms to further penetrate the alloy. This mechanism explains why the alloy with higher area percentage of the dark phase exhibits faster hydrogen absorption kinetics.[25–27]

3.5 Activation energy of hydrogen absorption and hydride decomposition

In order to investigate the activation energy of the hydrogen absorption of Ti_xFe_{2-x} (x = 1.1, 1.2, 1.3) alloys. The hydrogen absorption curves of three alloys at different temperatures were measured in Fig. 10(a–c). It can be seen that the hydrogen storage capacity of each alloy decreases with increasing the temperature. Table 5 lists the usual models of rate limiting step during the hydrogenation process,[28] where t is the reaction time, α is the fraction of reaction completion and k is the rate constant. The chemisorption model represents surface reaction. The JMA2D/3D model describes two-dimensional/three-dimensional nucleation with a constant interface velocity. The CV2D/3D model stands for two-dimensional/three-dimensional controlled volume shrinkage. The GB2D/3D model characterizes two-dimensional/three-dimensional diffusion and growth controlled by a continuously decreasing interface velocity.

Table 5 The usual models of rate limiting step during the hydrogenation process[28]

Model name	Model equation
Chemisorption	$\alpha = kt$
JMA2D	$[-\ln(1-\alpha)]^{1/2} = kt$
JMA3D	$[-\ln(1-\alpha)]^{1/3} = kt$
CV2D	$[1-(1-\alpha)]^{1/2} = kt$
CV3D	$[1-(1-\alpha)]^{1/3} = kt$
GB2D	$(1-\alpha)\ln(1-\alpha) + \alpha = kt$
GB3D	$1-(2\alpha/3)-(1-\alpha)^{2/3} = kt$

The representative hydrogen absorption curves of three alloys at 30 °C were fitted according to previous studies.[24–26] The fitting results are shown in Fig. 10(d–f). The adjusted R^2 values are listed in Table 6. As we know, the closer the adjusted R^2 value is to 1, the higher the degree of fit. From Table 6 and it is clear that three alloys agree with the GB3D model. The mechanism of hydrogen absorption is governed by three-dimensional diffusion and growth controlled by a continuously decreasing interface velocity.

After confirming that the mechanism of hydrogen absorption follows the GB3D model. The hydrogen absorption curves at three temperatures are fitted by using the GB3D model. The fitting results are shown in Fig. 11(a–c). The corresponding rate constants (K) and adjusted R^2 values for each temperature are listed in Table 7. The natural logarithm of the rate constant (ln k) is plotted against the reciprocal of temperature ($1/T$) and

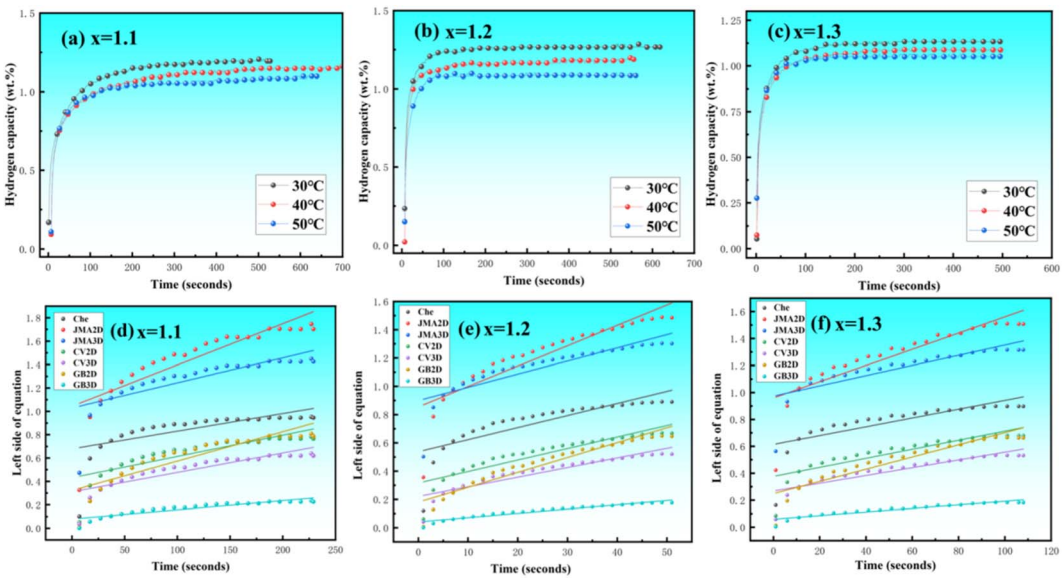

Fig. 10 The hydrogen absorption curves of Ti_xFe_{2-x} (x = 1.1, 1.2, 1.3) alloys at different temperatures (a–c). Fitted hydrogen absorption curves of Ti_xFe_{2-x} (x = 1.1, 1.2, 1.3) alloys at 30 °C (d–f).

Table 6 Adjusted R^2 values of the hydrogen absorption curves after fitting for three alloys

Samples	Che	JMA2D	JMA3D	CV2D	CV3D	GB2D	GB3D
$x = 1.1$	0.60806	0.82456	0.78292	0.78078	0.82971	0.82538	0.90681
$x = 1.2$	0.68705	0.82026	0.76696	0.82474	0.86357	0.90971	0.93507
$x = 1.3$	0.66715	0.82632	0.78159	0.81396	0.85454	0.88855	0.91739

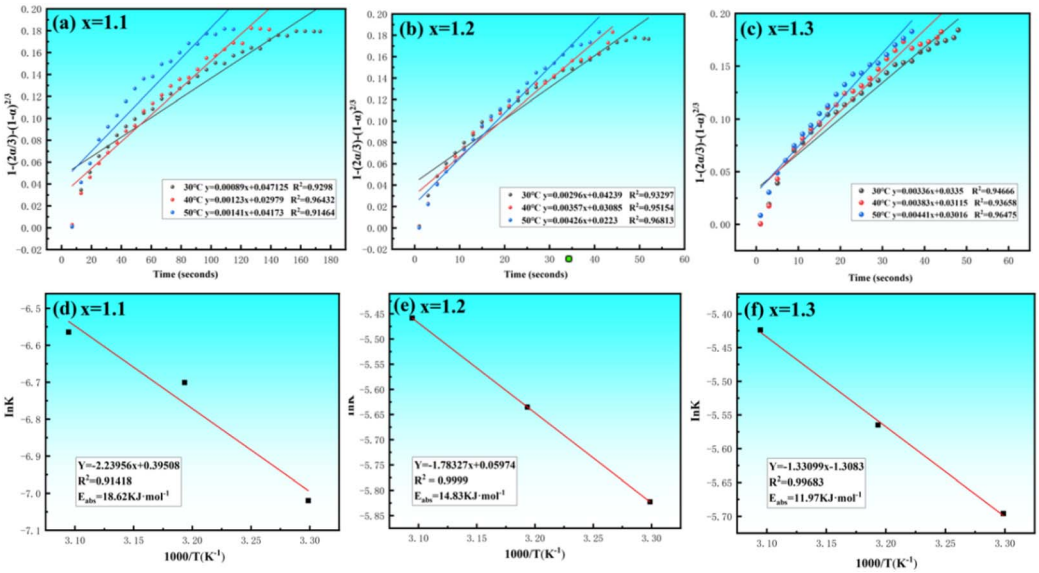

Fig. 11 GB3D-fitted hydrogen absorption curves of Ti_xFe_{2-x} ($x = 1.1, 1.2, 1.3$) alloys at different temperatures (a–c). Arrhenius fitting of Ti_xFe_{2-x} ($x = 1.1, 1.2, 1.3$) alloys (d–f).

fitted linearly as shown in Fig. 11(d–f). Using the Arrhenius eqn (1) and these parameters fitted.

$$\ln\ k = \frac{-E_a}{RT_p} + \ln\ A \quad (1)$$

The activation energies of hydrogen absorption of three alloys are calculated as 18.62, 14.83 and 11.97 kJ mol^{-1}, respectively. The result indicates that the activation energy decreases with increasing Ti content, suggesting that higher Ti content enhances hydrogen diffusion.

DSC was conducted to study the activation energy of hydride decomposition of two representative alloys ($x = 1.2$ and 1.3). For $x = 1.2$ and $x = 1.3$ alloys, the decomposition peak temperature is around 444.8 °C and 460.2 °C, respectively. Fig. 12(a and b) present DSC curves of $x = 1.2$ and $x = 1.3$ alloys under different heating rates. Based on the method proposed by Kudiiarov *et al.*,[29] the Kissinger eqn (2) was used to fit the decomposition peak temperature.

$$\ln\frac{\beta}{T_p^{\ 2}} = C - \frac{E_a}{RT_p} \quad (2)$$

The fitted curves are shown in Fig. 12(c and d). The calculated activation energies of hydride decomposition are 98.56 kJ mol^{-1} for $x = 1.2$ alloy and 126.97 kJ mol^{-1} for $x = 1.3$ alloy. It is clear that the activation energy of hydride decomposition increases with Ti content.

3.6 PCT properties

Fig. 13(a–c) shows PCT curves of Ti_xFe_{2-x} ($x = 1.1, 1.2, 1.3$) alloys at different temperatures. The plateau pressure of three alloys increases with the temperature, indicating that the hydrogen absorption reaction is exothermic. Using the method proposed by Liu *et al.*[30] and Cheng *et al.*,[31] PCT curves are fitted by Van't Hoff eqn (3) to determine the thermodynamic parameters, as shown in Fig. 13(e–f).

Table 7 Fitted K and adjusted R^2 values at different temperatures based on the GB3D model

Samples/Temperature	30 °C	40 °C	50 °C
$x = 1.1$	$K = 0.00089\ R^2 = 0.92980$	$K = 0.00123\ R^2 = 0.96432$	$K = 0.00141\ R^2 = 0.96464$
$x = 1.2$	$K = 0.00296\ R^2 = 0.93297$	$K = 0.00357\ R^2 = 0.95154$	$K = 0.00426\ R^2 = 0.96813$
$x = 1.3$	$K = 0.00336\ R^2 = 0.94666$	$K = 0.00383\ R^2 = 0.93658$	$K = 0.00441\ R^2 = 0.96475$

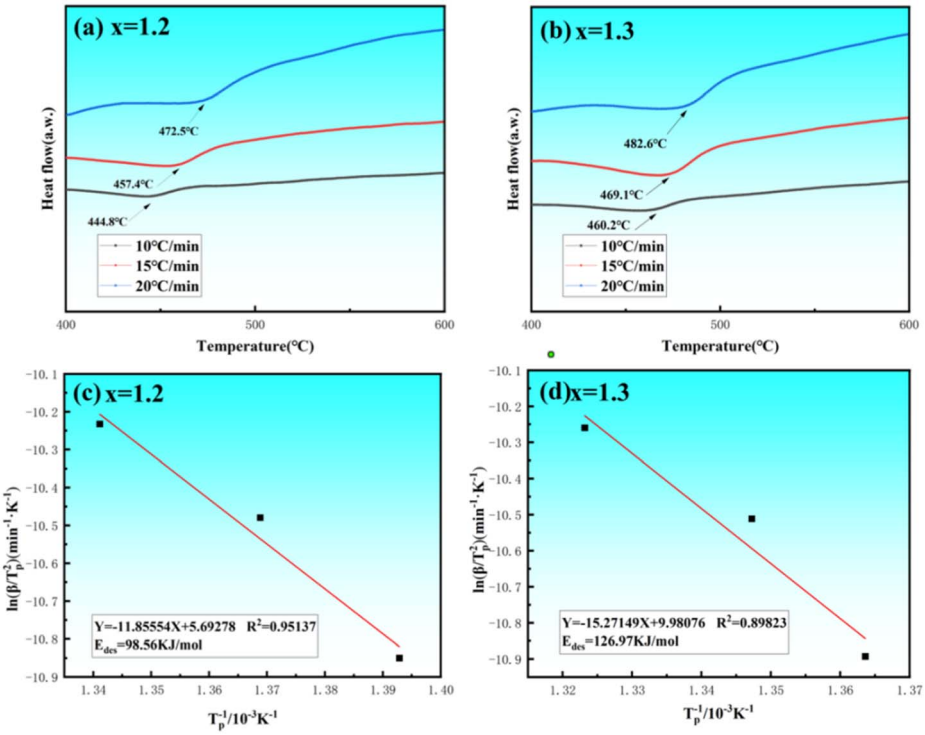

Fig. 12 DSC curves of $x = 1.2$ and $x = 1.3$ alloys at different heating rates (a and b). Fitted curves by using Kissinger equation of $x = 1.2$ and 1.3 alloys (c and d).

$$\ln\left(\frac{P_{ep}}{P_0}\right) = \frac{\Delta H}{RT} - \frac{\Delta S}{R} \quad (3)$$

The standard enthalpy of formation (ΔH) for the hydrides of three alloys is -17.59 kJ mol^{-1} ($x = 1.1$), -22.38 kJ mol^{-1} ($x = 1.2$) and -26.55 kJ mol^{-1} ($x = 1.3$). The absolute value of ΔH increases with Ti content. This result means the stability of alloy hydride increases with Ti content.

3.7 Oxidation resistance

Fig. 14(a and b) presents the first hydrogenation curves of $x = 1.1$ and $x = 1.3$ alloys after different air exposure time. It is clear that the maximum hydrogen storage capacity decreased with the increase of air exposure time. When the air exposure time is 2 h, the $x = 1.3$ alloy can't absorb hydrogen again within 30 000 s. Fig. 14(c) shows the incubation time of the first hydrogenation of $x = 1.1$ and $x = 1.3$ alloys after different air exposure time. The incubation time of $x = 1.1$ alloy increases from

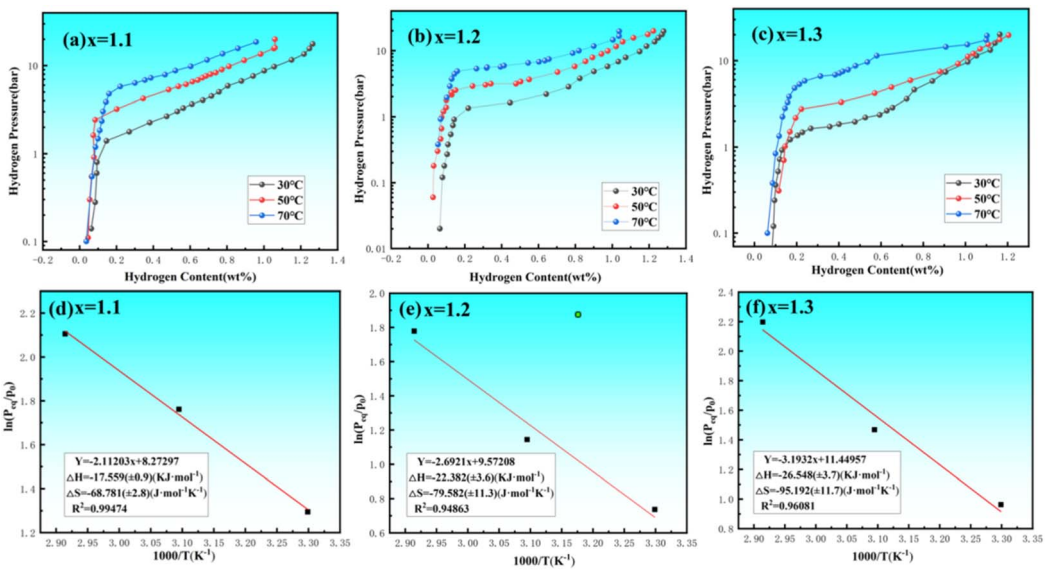

Fig. 13 PCT curves at different temperatures (a–c) and Van't Hoff fitting plots for Ti_xFe_{2-x} ($x = 1.1$, 1.2, 1.3) alloys (d–f).

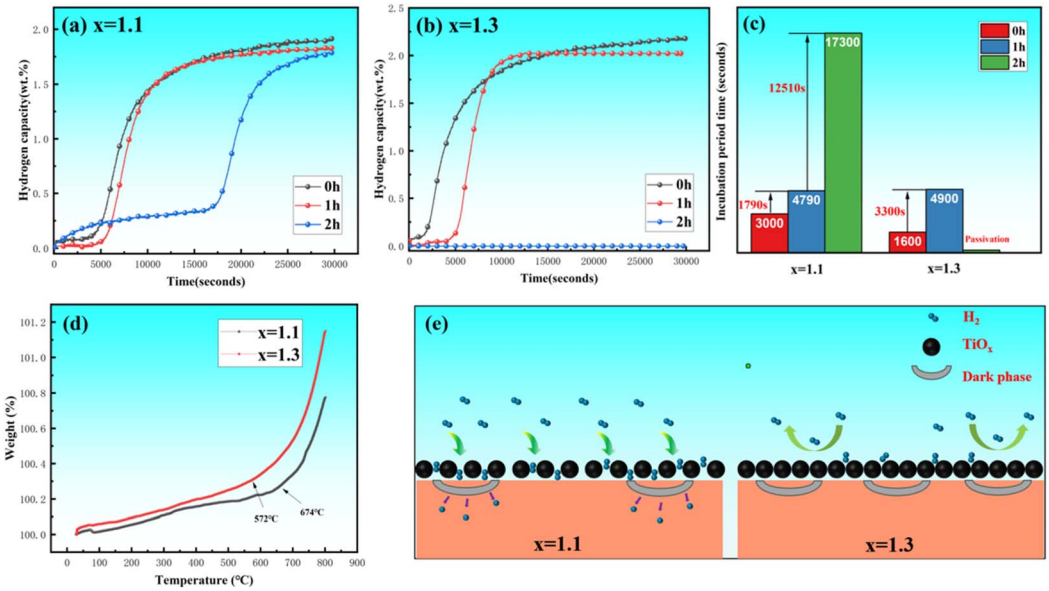

Fig. 14 Hydrogen absorption curves of $x = 1.1$ (a) and $x = 1.3$ (b) alloys after different air exposure time. Comparison chart of the incubation time (c). TG curves of $x = 1.1$ and $x = 1.3$ alloys (d). Illustration of the mechanism of hydrogen absorption of the alloy after air exposure (e).

around 3000 s (without air exposure) to around 4790 s (after 1 h of air exposure) and around 17 300 s (after 2 h of air exposure). In contrast, the $x = 1.3$ alloy exhibits a more pronounced degradation. Its incubation time rises from around 1600 s (without air exposure) to around 4900 s (after 1 h of air exposure). After 2 h of air exposure, the $x = 1.3$ alloy is dead totally. This suggests that the $x = 0.3$ alloy is sensitive to the air. Fig. 14(d) shows TG curves of $x = 1.1$ and $x = 1.3$ alloys. The $x = 1.3$ alloy exhibits a much greater weight increase than that of $x = 1.1$ alloy. This result also further confirms the $x = 1.3$ alloy has poorer oxidation resistance. This reason might be attributed to the fact that Ti is more prone to oxidation than Fe.[32] Ti can react easily with the oxygen to form TiO_x. For $x = 1.3$ alloy, its higher Ti content accelerates the process of surface oxidation and promotes the growth of an oxide layer on its surface.[21]

The mechanism of hydrogen absorption of the alloy after oxidation can be predicted in Fig. 14(e). As we know from Table 4, the dark phase has a higher Ti content on its surface than the bright phase. When the alloy is exposed to air, an oxide film forms on the surface of the bright phase firstly. In addition, the area percentage of the dark phase increases with Ti content. The higher the content of Ti is, the more oxide layer there will be on the surface of the alloy. As the air exposure time increases, the oxide layer becomes thicker. The oxide layer formed in air can block the channel for hydrogen diffusion. This explains why the longer the same alloy is exposed to air, the longer its incubation time.[33,34]

4 Conclusions

This study systematically investigated the effect of regulating the ratio of Ti and Fe elements on the microstructure, hydrogenation, thermodynamic properties and oxidation resistance of Ti_xFe_{2-x} ($x = 1$, 1.1, 1.2, 1.3) alloys. From the perspective of the microstructure, all as-cast alloys contain TiFe main phase and Ti_2Fe secondary phase except $x = 1$ alloy. In addition, excessive Ti promotes the formation of Ti_2Fe secondary phase and results in the expansion of lattice parameter, unit cell volume and crystallite size of TiFe main phase. In addition to this, all as-cast alloys show the bright and dark phases. The area percentage of the dark phase increases with Ti content. From the perspective of the hydrogenation properties, increasing Ti content can enhance the first hydrogenation kinetics and rise the maximum hydrogen storage capacity from 1.91 wt% ($x = 1.1$) to 2.27 wt% ($x = 1.3$). This may be due to the dark phase formed that is helpful for hydrogen dissociation and diffusion. But the reversible hydrogen storage capacity decreases from 1.37 wt% ($x = 1.1$) to 1.10 wt% ($x = 1.3$). This reason may be because the excessive Ti reacts with hydrogen to form stable TiH_x hydrides. From the perspective of the thermodynamic properties, the activation energies of hydrogen absorption are calculated as 18.62 ($x = 1.1$), 14.83 ($x = 1.2$) and 11.97 kJ mol^{-1} ($x = 1.3$), respectively. The result indicates that higher Ti content enhances hydrogen diffusion. The activation energies of hydride decomposition are 98.56 kJ mol^{-1} for $x = 1.2$ alloy and 126.97 kJ mol^{-1} for $x = 1.3$ alloy. The activation energy of hydride decomposition increases with Ti content. The standard enthalpy of formation (ΔH) of the hydrides is −17.59 ($x = 1.1$), −22.38 ($x = 1.2$) and −26.55 kJ mol^{-1} ($x = 1.3$). This result means the stability of alloy hydride increases with Ti content. From the perspective of the oxidation resistance, the oxidation resistance decreases with increasing Ti content. This reason might be attributed to the fact that Ti is more prone to oxidation than Fe.

Conflicts of interest

All of the authors declare that they have no conflicts of interest that are relevant to the content of this article.

Abbreviation

XRD	X-ray diffraction
SEM	Scanning electron microscope
EDS	Energy dispersive X-ray spectroscopy
DSC	Differential scanning calorimetry
TGA	Thermogravimetric Analysis
DTG	Differential thermogravimetry
PCT	Pressure-composition-temperature
JMA	Nucleation-growth-impingement model
CV	Contracting volume model
GB	Ginstling-Brounshtein model

Data availability

The data and materials presented in this study are available on request from the corresponding author. The data are not publicly available due to privacy restrictions.

Supplementary information (SI) is available. See DOI: https://doi.org/10.1039/d5ra09388k.

Acknowledgements

This work is supported by National Natural Science Foundation of China (12205042), Jiangxi Provincial Natural Science Foundation (20252BAC240176), Engineering Research Center of Nuclear Technology Application, Ministry of Education (HJSJYB2022-6), Science and Technology Research Project of Jiangxi Provincial Department of Education (GJJ2200762), East China University of Technology (ECUT) for PhD research fund and experimental technology project (DHBK2022008) and Graduate Innovation Fund of East China University of Technology (DHYC-2025140 and DHYC-2025141).

References

1 C. A. Mirkin, E. H. Sargent and D. P. Schrag, Energy transition needs new materials, *Science*, 2024, **384**(6697), 713–719.
2 T. Pakulska, The Energy Crisis—Looking at the Renewable Transition, *Energies*, 2023, **16**(15), 5705.
3 A. Mehrabianbardar, M. Shirinbayan, Z. Jendli, *et al.*, A review: challenges, processes, and innovations in high-pressure hydrogen storage technologies, *Int. J. Material Form.*, 2025, **18**(3), 77.
4 M. D. Allendorf, V. Stavila, J. L. Snider, *et al.*, Challenges to developing materials for the transport and storage of hydrogen, *Nat. Chem.*, 2022, **14**(11), 1214–1223.
5 G. Chen, D. Liang, Z. Kang, *et al.*, Review of Hydrogen Storage in Solid-State Materials, *Energies*, 2025, **18**(11), 2930.
6 J. J. Reilly and R. H. Wiswall, Formation and properties of iron titanium hydride, *Inorg. Chem.*, 1974, **13**(1), 218–222.
7 J. Barale, E. M. Dematteis, G. Capurso, *et al.*, TiFe0.85Mn0.05 alloy produced at industrial level for a hydrogen storage plant, *Int. J. Hydrogen Energy*, 2022, **47**(69), 29866–29880.
8 W. R. Naotoyasuda, S. Sasaki, *et al.*, Self-ignition combustion synthesis of TiFe1−xMnx hydrogen storage alloy, *Int. J. Hydrogen Energy*, 2009, **34**(22), 9122–9127.
9 K. B. Park, W.-S. Ko, J. O. Fadonougbo, *et al.*, Effect of Fe substitution by Mn and Cr on first hydrogenation kinetics of air-exposed TiFe-based hydrogen storage alloy, *Mater. Charact.*, 2021, 178.
10 C. Gosselin and J. Huot, Hydrogenation Properties of TiFe Doped with Zirconium, *Materials*, 2015, **8**(11), 7864–7872.
11 V. Razafindramanana, S. Gorsse, J. Huot and J. L. Bobet, Effect of Hafnium Addition on the Hydrogenation Process of TiFe Alloy, *Energies*, 2019, **12**, 3477.
12 K. Komędera, J. M. Michalik, K. Sworst, *et al.*, Structure, Microstructure and Hyperfine Interactions in Hf- and Ni-Substituted TiFe Alloy for Hydrogen Storage, *Acta Physica Polonica A*, 2024, 215–221.
13 J. Y. Jung, S.-I. Lee, M. Faisal, *et al.*, Effect of Cr addition on room temperature hydrogenation of TiFe alloys, *Int. J. Hydrogen Energy*, 2021, **46**(37), 19478–19485.
14 Y. Li, H. Xiao, M. Zhong and Q. Chen, Effect of Cr and Mo Substitution of Fe on Activation and Hydrogen Ab-/Desorption Properties of TiFe Hydrogen Storage Alloy, *Metals*, 2025, **15**, 200.
15 J. Manna and J. Huot, Effect of KCl Addition on First Hydrogenation Kinetics of TiFe, *Compounds*, 2022, **2**, 240–251.
16 H. Emami, K. Edalati, J. Matsuda, *et al.*, Hydrogen storage performance of TiFe after processing by ball milling, *Acta Mater.*, 2015, **88**, 190–195.
17 L. E. R. Vega, D. R. Leiva, R. M. Leal Neto, *et al.*, Mechanical activation of TiFe for hydrogen storage by cold rolling under inert atmosphere, *Int. J. Hydrogen Energy*, 2018, **43**(5), 2913–2918.
18 M. W. Davids, M. Lototskyy, A. Nechaev, *et al.*, Surface modification of TiFe hydrogen storage alloy by metal-organic chemical vapour deposition of palladium, *Int. J. Hydrogen Energy*, 2011, **36**(16), 9743–9750.
19 C. Peng, D. Huang, Q. Liu, *et al.*, In Situ Preparation of Nickel Nanoparticles and Their Effects on the Hydrogen Storage Properties and Oxidation Resistance of Ti–Fe–Mn-Zr Alloy, *ACS Appl. Energy Mater.*, 2025, **8**(10), 6423–6441.
20 K. B. Park, W.-S. Ko, J. O. Fadonougbo, *et al.*, Effect of Fe substitution by Mn and Cr on first hydrogenation kinetics of air-exposed TiFe-based hydrogen storage alloy, *Mater. Charact.*, 2021, **178**, 111246.
21 K. B. Park, T.-W. Na, Y. D. Kim, *et al.*, Characterization of microstructure and surface oxide of Ti1.2Fe hydrogen storage alloy, *Int. J. Hydrogen Energy*, 2021, **46**(24), 13082–13087.
22 E. Ulate-Kolitsky, B. Tougas and J. Huot, First Hydrogenation of TiFe with Addition of 20 wt.% Ti, *Hydrogen*, 2022, **3**(4), 379–388.
23 K. Edalati, E. Akiba and Z. Horita, High-pressure torsion for new hydrogen storage materials, *Sci. Technol. Adv. Mater.*, 2018, **19**(1), 185–193.
24 D. Bellon Monsalve, E. Ulate-Kolitsky, J. M. Cubero-Sesin, *et al.*, Microstructure and First Hydrogenation Properties

of Individual Phases in TiFe + 12 wt.% ZrV2 Alloy, *ChemEngineering*, 2024, **8**(4), 81.

25 K. Li, B. Tang, M. Zhang, *et al.*, A hydrogen diffusion model considering grain boundary characters based on crystal plasticity framework, *Int. J. Plast.*, 2023, **169**, 103740.

26 Y. Niu, T. Li, Z. Yuan, *et al.*, An overview of TiFe-based alloys for hydrogen storage: structure, element substitution and preparation, *Int. J. Hydrogen Energy*, 2025, **175**, 151503.

27 J. Qiu, H. Wan, Z. Ding, *et al.*, Tailoring hydrogen diffusion pathways in Mg-Ni alloys through Gd addition: A combined experimental and computational study, *Chem. Eng. J.*, 2024, **502**, 157767.

28 C. Peng, Q. Liu, P. Lv, *et al.*, Tailoring hydrogenation and anti-oxidation properties of titanium - iron - chromium alloys by regulating zirconium content at room temperature, *Int. J. Hydrogen Energy*, 2023, **48**(97), 38374–38388.

29 V. N. Kudiiarov, A. Kenzhiyev, N. Kurdyumov, *et al.*, Superior catalytic activity of nano sized Ni produced by electrical explosion of wires towards the hydrogen storage of magnesium hydride, *Int. J. Hydrogen Energy*, 2025, **109**, 436–452.

30 Y. Liu, L. Xiong, B. Gao, *et al.*, Enhanced hydrogen kinetics of Mg–Ni–La alloys via slight Y element additive, *Int. J. Hydrogen Energy*, 2024, **86**, 835–843.

31 B. Cheng, L. Kong, H. Cai, *et al.*, Exploring microstructure variations and hydrogen storage characteristics in TiVNbCrNi high-entropy alloys with different Ni incorporation, *Int. J. Hydrogen Energy*, 2024, **72**, 29–40.

32 P. Den Hoed and A. Luckos, Oxidation and Reduction of Iron-Titanium Oxides in Chemical Looping Combustion: A Phase-Chemical Description, *Oil Gas Sci. Technol.*, 2011, **66**, 249–263.

33 Z. Huang, Z. Yao, Y. Cui, *et al.*, Influence of Ti-Rich Secondary Phase on the Hydrogen Storage Performance of V-Based Hydrogen Storage Alloys, *Energy Fuels*, 2024, **38**(13), 12121–12128.

34 K. Edalati, J. Matsuda, M. Arita, *et al.*, Mechanism of activation of TiFe intermetallics for hydrogen storage by severe plastic deformation using high-pressure torsion, *Appl. Phys. Lett.*, 2013, **103**(14), 143902.